A Hybrid Silica Nanoreactor Framework for Encapsulation of Hollow Manganese Oxide Nanoparticles of Superior T_1 Magnetic Resonance Relaxivity

Benedict You Wei Hsu, Michael Ng, Yu Zhang, Siew Yee Wong, Kishore Bhakoo, Xu Li, and John Wang**

A new hybrid nanoreactor framework with poly(ethylene oxide)-perforated silica walls is designed to encapsulate hollow manganese oxide nanoparticles (MONs) of high distinctness and homogeneity. Achieved by an interfacial templating scheme, the nanoreactor ensures that acidic etching of MONs by an acetate buffer solution is highly controlled for precise control of the hollow interior. As such, hollow MONs with different nanostructures are developed successfully through a facile acetate buffer solution etching. The resultant hollow MONs are integrated within the hybrid nanoreactor and demonstrate superior r_1 relativity of up to 2.58 mM^{-1} s^{-1} for T_1 magnetic resonance imaging (MRI). By modifying the nanoreactor architecture, it is also demonstrated that the efficacy of MONs as T_1 MRI contrast agents can be significantly improved if an optimal cluster of hollow MONs is encapsulated into the hybrid silica framework. The evolution of core morphology with time is studied to elucidate the etching mechanism. It is revealed that the hollow formation arises due to the surface stabilization of MONs by acetate ions and the subsequent acidic etching of the interior core in a sporadic manner. This is different from the commonly reported nanoscale Kirkendall effect or the selective etching of the core–shell MnO/Mn_3O_4 structure.

1. Introduction

In 2007, Hyeon and co-workers published their seminal work describing the use of manganese oxide nanoparticles (MONs) as T_1 contrast agents for magnetic resonance imaging (MRI).[1] Since then, this new class of MRI contrast agent has opened a new direction for exploring various strategies to engineer MONs of higher r_1 relaxivity. In this regard, modifying the particle size and morphology of MONs has been shown to have a significant effect on the r_1 relaxation rate. In general, the r_1 relaxivity is expected to increase as the particle size of MONs decreases. For example, Chen and co-workers found that MONs with a size of 10 nm exhibited a greater positive contrast ability than those with larger sizes.[2] Hollow-structured MONs are also attractive candidates as T_1 contrast agents because they exhibit high surface-to-volume ratio. Since only the surface Mn^{2+} ions in a nanoparticle are largely responsible for the longitudinal water proton relaxation, these hollow MONs tend to exhibit higher r_1 relaxivities than those of their solid counterparts. Herein, there has been a burgeoning interest to use hollow MONs as a platform to build an integrated MRI diagnostic and therapeutic nanoprobe for various types of cancers.[3–7]

There are a number of synthesis protocols that have been developed to produce the hollow cavities of MONs. Typically, they involve the selective core removal of presynthesized MONs by using a suitable etchant. Lee and co-workers used phthalate buffer solution at pH 4.6 to form the voids in the core of MONs.[3] Similarly, Gilad and co-workers employed mild hydrochloric acid solution at pH 2.4 to extrude the hollow core of MONs.[4] Such approaches were successful due to a compositional difference between the core and shell of MONs. As a result, the hollow interior is created by a preferential dissolution of the MnO core phase and the stability of the Mn_3O_4 shell phase under acidic conditions. Alternatively, a hydroxylamine (NH_2OH) dispersion, which is known to form complexes with metal ions readily, has been demonstrated to be effective in the selective etching of MnO core from a sacrificial template of MnO-Mn_3O_4 core–shell nanoparticles, thus yielding well-defined hollow MONs.[8]

B. Y. W. Hsu
NUS Graduate School for Integrative Sciences and Engineering
National University of Singapore
28 Medical Drive, 117456, Singapore
M. Ng, Prof. K. Bhakoo
Translational Molecular Imaging Group
Singapore Bioimaging Consortium (SBIC)
Agency for Science, Technology and Research (A*STAR)
11 Biopolis Way, 02-02 Helios 138667, Singapore
Dr. Y. Zhang, Prof. J. Wang
Department of Materials Science & Engineering
National University of Singapore
9 Engineering Drive 1, 117576, Singapore
E-mail: msewangj@nus.edu.sg
S. Y. Wong, Dr. X. Li
Institute of Materials Research and Engineering (IMRE)
Agency for Science, Technology and Research (A*STAR)
3 Research Link, 117602, Singapore
E-mail: x-li@imre.a-star.edu.sg

DOI: 10.1002/adfm.201501269

© 2015 WILEY-VCH Verlag GmbH & Co. KGaA, Weinheim

Apart from the composition difference-based selective etching strategy, the nanoscale Kirkendall effect is another method that is commonly used to produce hollow MONs. It provides a mechanism for void formation in inorganic nanoparticles because the outward diffusion of Mn^{2+} ions is balanced by an inward flux of vacancies which would subsequently coalesce to form the hollow interior core. During the formation process, the surface layer of MONs is usually stabilized by surfactants or simple inorganic anions in the solution. This reduces the overall surface energies and promotes the spontaneous dissolution of the particle interiors. For example, Chou and co-workers have identified that the acetate anion is crucial to the structural evolution from solid to hollow MONs in their synthesis protocol, as it can function as a chelating ligand to remove the MnO core via the Kirkendall effect.[5] Hyeon and co-workers have also attributed their success of preparing hollow MONs to the Kirkendall effect, wherein the alkylphosphonic acid impurities in technical grade trioctylphosphine oxide (TOPO) are able to bind strongly to the surface Mn^{2+} ions and drive the hollowing process of MONs.[9]

However, despite the recent advances in developing hollow MONs, there has been limited work done to tailor the architecture of hollow nanostructures. In fact, to the best of our knowledge, reports on the synthesis of hollow MONs are primarily focused on single particle encapsulation. In this regard, perhaps there is a notion that individually encapsulated hollow MONs are able to induce the longitudinal water proton relaxation most efficiently. Otherwise, it may be challenging to control the size and uniformity of the encapsulation of hollow MONs clusters.[10] Therefore, we report a hybrid silica nanoreactor for the facile synthesis of well-defined hollow MONs. The framework itself is composed of a thin silica nanoshell that is perforated by the poly(ethylene oxide) (PEO) chains of F127. Using these nanocontainers to encapsulate MONs, several key advantages become apparent: besides eliciting a relatively high r_1 relaxivity due to an improved accessibility of water molecules to the encapsulated MON core, the nanoreactor framework can also provide the desired in situ surface modification by substituting the hydrophobic oleate ligands of MONs with highly hydrophilic PEO chains that resist reticuloendothelial system interactions.[11] Hence, the blood circulation time of MONs can be prolonged for better MRI visualization.[12] Indeed, such useful properties have been validated in our previous study, which demonstrated the excellent antifouling behaviour and high water permeability of the PEO-perforated silica nanoshell.[11] On the basis of these results, in the present study, the hybrid silica nanocapsules were employed as robust nanoreactors to prepare hollow MONs of various architectures (single or a cluster of core particles). Moreover, we demonstrate a novel approach to increase the r_1 relaxivities of MONs, wherein a moderate number of core nanoparticles are encapsulated to increase the rate of water exchange. Thus, this will favor a further development of MONs as T_1 contrast agents in clinical applications.

2. Results and Discussion

2.1. Nanoreactor Synthesis of Hollow MONs

Hydrophobic MONs are first synthesized by the thermal decomposition of manganese oleate complex in organic solvents of high boiling point. Transmission electron microscopy (TEM) study reveals that the MONs are highly uniform in particle size. By changing the reaction temperature, type of solvent, or reaction time, the MONs could be tailored to a range of sizes (Figure S1a, Supporting Information). X-ray diffraction (XRD) analysis indicated that the phase purity of MnO was maintained despite their varying particle sizes (Figure S1b, Supporting Information). This was verified by the SAED pattern as the diffraction rings were consistent with the structure of MnO (Figure S1c, Supporting Information). Compared to the commonly used 1-hexadecene and 1-octadecene solvents,[1–9] smaller MONs are readily yielded when the hydrocarbon chain length of the alkene solvent is reduced. It is noteworthy that highly monodispersed sub 10 nm MONs are formed by employing 1-tetradecene as the solvent of high boiling point in our synthesis protocol. This could be ascribed to a higher degree of solvent stabilization provided by the shorter chain alkene, thus increasing the thermal stability of manganese oleate complex. Hence, in accordance with the LaMer model, its decomposition kinetics would occur at a higher temperature and lead to the formation of a large amount of MnO nuclei but of smaller radii.[13]

Interfacial templating condensation of TMOS in the core–shell region of F127 micelles was employed to fabricate the hybrid silica nanoreactor.[11] Herein, in order to provide a direct comparison with earlier reports on hollow MONs, which typically range from 15 to 20 nm in sizes, we chose the 16 nm-sized MONs for encapsulation into our hybrid silica nanoreactors. Next, to form the hollow core of MONs, we employed an acidic acetate buffer solution (pH 5.2) as the etchant under standard temperature and pressure. This is crucial to generate the well-defined hollow morphology of MONs. The versatility of this method is demonstrated by the facile synthesis of hollow MONs with varying encapsulation morphologies. **Scheme 1** shows an outline for the preparation of hollow MONs using our nanoreactor platform.

2.2. Designing MONs of Higher r_1 Relaxivity

There are three key advantages in employing our nanoreactor platform for the development of hollow MONs. First, by employing the interfacial templating technique, hydrolysis and condensation of silica precursors are confined to the interface between the poly(propylene oxide) (PPO) core and PEO corona of the polymeric micelles. Hence, the nanoreactors are composed of a thin silica shell that is perforated with PEO chains (**Figure 1**), which enable them to maintain their structural integrity and aqueous dispersity in the etchant solution for a prolonged duration of time. This is in contrast to other designs of silica-coated hollow MONs, which tend to require the direct coating of a thick silica layer onto the MONs prior to nanoscale etching.[4,5,8] Such enhanced stability of our framework is attributed to its nanocomposite-type structure, where the inorganic silica fractions yield mechanical strength and the hydrophilic PEO chains provide good antifouling properties. Second, the silica nanoreactor provides a high degree of control over the hollow nanostructure of MONs as it ensures that the etching chemistry is done in a confined volume under

© 2015 WILEY-VCH Verlag GmbH & Co. KGaA, Weinheim

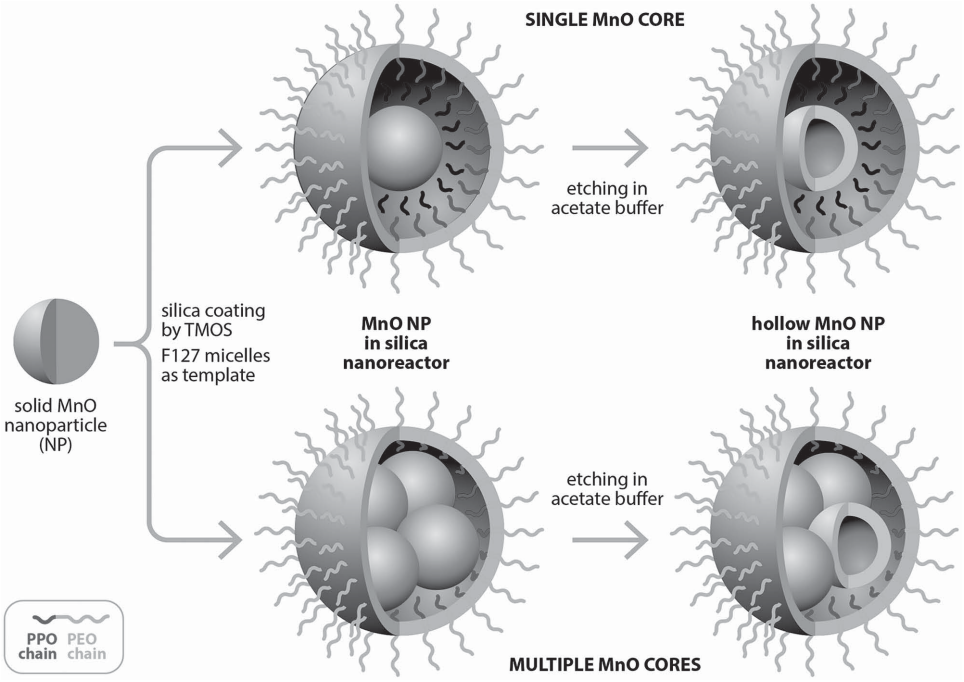

Scheme 1. Schematic illustration for the synthesis of hollow MONs.

controlled conditions and selective permeability. This is due to the controlled diffusion of etchant molecules through the PEO-based polymer nanochannels that perforated through the silica shell. The permeability of the silica shell is confirmed by the subsequent diffusion of Mn^{2+} ions from the nanoreactor during etching, which is elaborated further in the later section. Third, due to the employment of F127 polymeric micelles as soft templates to form the silica shell, the dimensions of our nanoreactor construct can be facilely altered in accordance to the number of encapsulated MONs. This allows for a systematic investigation into the nanocomposite architecture in order to engineer MRI contrast agents of higher r_1 relaxivity. There are two parameters that are varied: i) MON core morphology (solid vs hollow nanoparticles); ii) Number of MONs (single vs multiple nanoparticles). **Table 1** shows the r_1 relaxivities of the samples. Plots of the T_1^{-1} versus Mn concentration for the hollow MONs can be found in Figure S2 (Supporting Information).

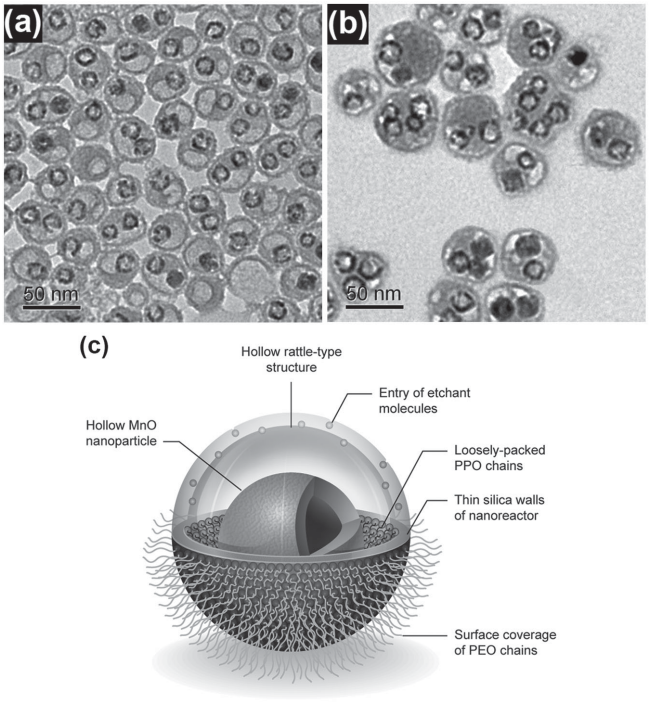

Figure 1. TEM images of the hollow MONs with: a) single 16 nm core and b) multiple 16 nm cores. c) 3D-illustration of the hybrid silica nanoreactor framework.

Our relaxivity measurements indicate that the formation of a hollow interior is indeed a useful strategy to enhance the r_1 relaxivity of MONs. This can be explained by the increased concentration of surface Mn ions that is exposed to water molecules in the inner surface.[3,4] Interestingly, there is also a consistent increase in the r_1 relaxivities of MONs if there is a cluster encapsulation of core particles. In fact, among all of the various nanocomposite architectures of MONs, the hollow MONs with multiple 16 nm cores exhibit the highest r_1 relaxivity of 2.58×10^{-3} M^{-1} s^{-1} (Table 1). This r_1 value is more than a two-fold increase when compared to the hollow MONs with only a single 16 nm core, as reflected in their corresponding T_1-weighted images (**Figure 2**a). Although the relaxivity is lower when compared to commercial T_1 reagents (Magnevist, Gd-DTPA), which exhibits a r_1 value of 5.33×10^{-3} M^{-1} s^{-1} at 7 T under the same testing conditions (Figure S3, Supporting Information), the nanosystem represents an alternative class of T_1 MRI contrast agents that offers lower toxicity and comparable imaging performance, especially in view of the recent association of gadolinium-based contrast agents (GBCAs) with nephrogenic systemic fibrosis.[14,15] In vivo validation of the

© 2015 WILEY-VCH Verlag GmbH & Co. KGaA, Weinheim

Table 1. r_1 relaxivities of MONs with different nanostructures.

Core size [nm]	Core morphology	No. of core particles	r_1 value [$\times 10^{-3}$ M^{-1} s^{-1}]
16	Hollow	Multiple[a)]	2.58
16	Hollow	Single[b)]	1.23
16	Solid	Multiple	2.22
16	Solid	Single	1.17

[a)]Average number of MnO cores (2 or more); [b)]Average number of MnO cores (1 to 2).

hollow MONs with multiple 16 nm cores is also carried out by a subcutaneous injection of the nanoparticles (0.40×10^{-3} M) in the flank region of a mouse model (site **b**). A hyperintense region generated by the nanoparticles was observed in the transplantation site (Figure 2b), thus demonstrating their ability to function as highly efficient T_1 MRI contrast agents. The T_1 contrast enhancement as exerted by the cluster encapsulation can be explained by the rotational dynamics of MONs in the silica nanoreactor. Based on the Solomon–Bloembergen–Morgan (SBM) theory, the proton relaxation in paramagnetic solutions is highly dependent on the effective correlation time of the contrast agent, which should correspond closely to the proton Larmor precession frequency for an optimal r_1 relaxivity.[16,17] One method of modulating the effective correlation time is to control the rotational motion of the T_1 contrast agent.[18] For example, the rapid molecular rotation of free chelated Gd can be markedly slowed down by means of conjugation to a nanovesicle surface, thus achieving a higher

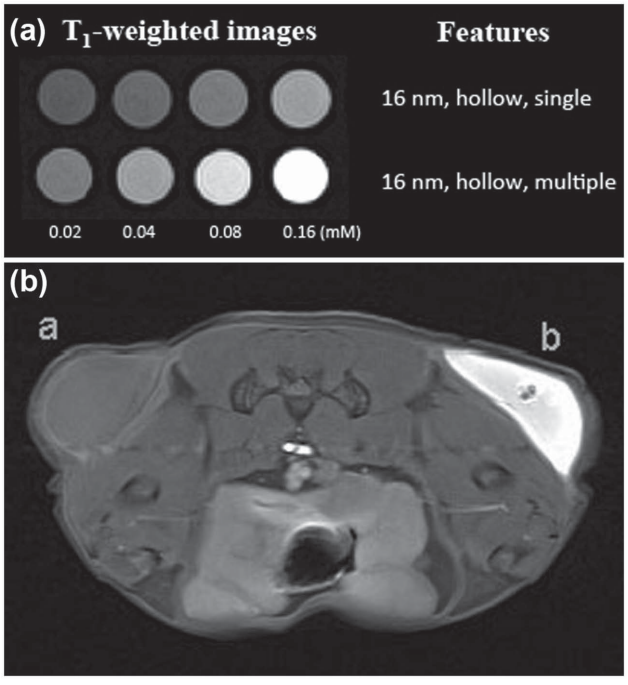

Figure 2. a) T_1-weighted MR images of the hollow MONs with different numbers of core particles. b) T_1-weighted image of a mouse with subcutaneous injection of 1% agarose (site **a**) (reference) and hollow MONs in 1% agarose (site **b**).

r_1 relaxivity.[19] In the present case, due to the higher particle packing density for the cluster encapsulation of MONs in the cavity of the silica nanoreactor, the rotational diffusion of surface Mn^{2+} ions of MONs is likely to be more restricted by the closer proximity and stronger interactions with the polar hydroxyl groups of the silica nanoshell. As a result, there is an increase in the rotational correlation time of the paramagnetic payload to a rate that more closely matches the proton Larmor frequency. In turn, this will induce a higher degree of T_1 relaxation to the surrounding water protons for enhanced T_1 MRI contrast.

A systematic investigation into the degree of T_1 contrast enhancement by samples with varying numbers of MONs was also conducted. The rationale of this study was to compare the measured relaxivities of each sample and determine if there is an ideal cluster size that corresponds to the optimal correlation time required to maximise the r_1 relaxivity of our system. The increasing number of MONs of each sample was verified by TEM and dynamic light scattering (DLS) analysis (**Figure 3**). The relaxation times of each sample were also measured on a preclinical 7.0 T MRI scanner. Figure 3f shows that the highest r_1 relaxivity is achieved when a moderate number of ≈3 MONs are encapsulated. Beyond this optimal cluster size, there is a gradual decrease in r_1 relaxivity with increasing number of core particles. Hence, these experimental results are in agreement with simulations which suggest that an intermediate rotational correlation time is required to maximize the r_1 relaxivity at fields of 1.5 T or higher.[18]

In addition to the influence of correlation time, it is also noteworthy that the paramagnetic relaxation enhancement of MONs can be divided into two different solvation spheres; namely inner and outer.[17] The inner sphere effect, which requires direct contact between the MONs and water molecules, is able to induce the proton relaxation rate more efficiently. Since the hybrid silica nanoreactor is able to allow water molecules to transverse through its PEO-perforated walls and interact directly with the MONs, the inner sphere relaxation is dominant and this accounts for the high r_1 relaxivities of MONs. However, upon the encapsulation of an excess number of MONs (i.e., ten particles or greater), there is less available space in the interior cavity of the nanoreactor for water molecules to diffuse into. This reduces the number of water molecules that can come into close proximity to the MONs and diminishes the influence of inner sphere relaxation, thereby lowering the r_1 relaxivity of MONs.

2.3. Kinetics of Hollow MON Formation

The evolution of core morphology with time was investigated to determine the etching mechanism in the nanoreactor framework. It is known that the Kirkendall effect should be reflected by an inward flow of vacancies to form voids, which tend to nucleate at the boundary due to its higher surface energy and defect content.[20,21] However, TEM images (**Figure 4**a) indicate an absence of Kirkendall intermediates with yolk–shell nanostructures. It is thus highly improbable that the nanoscale Kirkendall effect is responsible for driving the hollowing process in our system. Instead, the selective dissolution of the

© 2015 WILEY-VCH Verlag GmbH & Co. KGaA, Weinheim

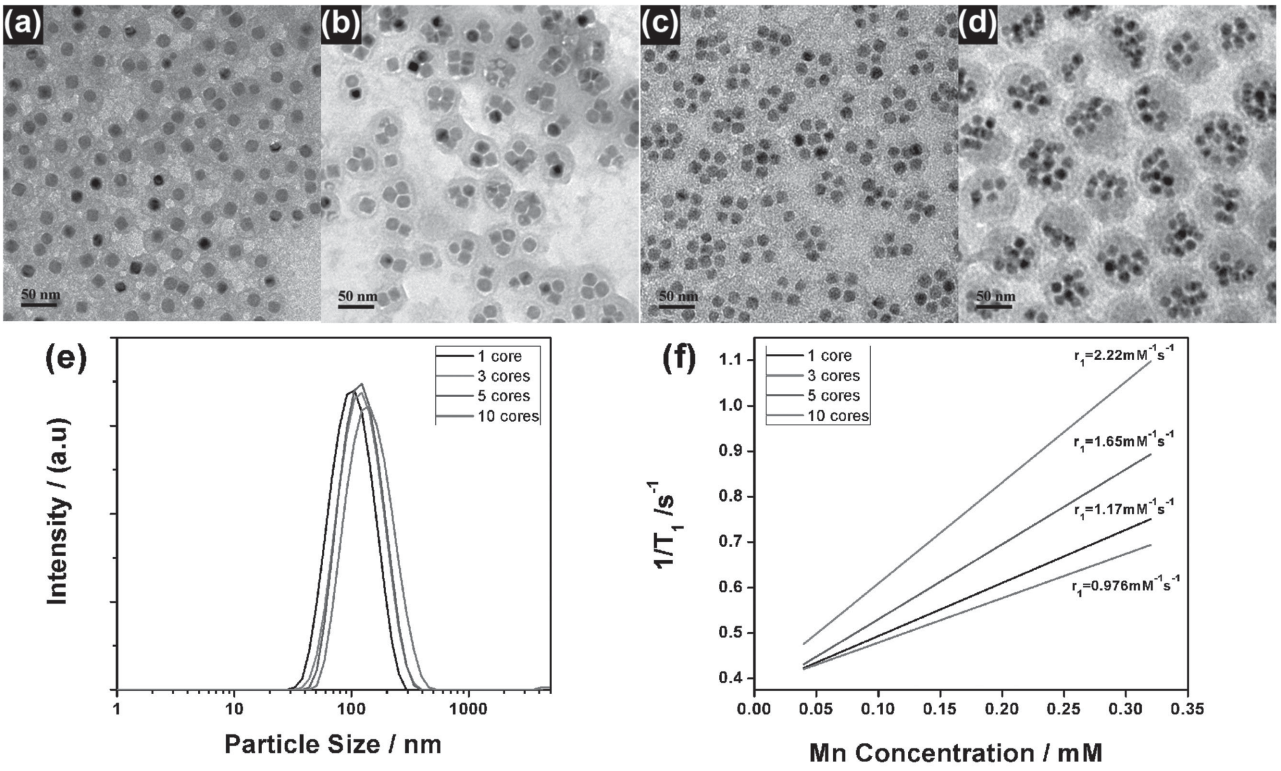

Figure 3. TEM images of the MONs prior to nanoscale etching, with a) one; b) three; c) five; d) ten core particles. The average number of core particles is based on a statistical assembly of 100 nanoparticles under TEM and indexed to the nearest integer. e) Hydrodynamic size distribution and f) plot of $1/T_1$ versus Mn concentration for the MONs of different cluster sizes.

nanoparticle interior has occurred in a sporadic and random manner, while a thin edge wall of about 3 nm has remained intact during the etching process, even after a prolonged etching duration of 48 h which ultimately causes the nanoreactor framework to disintegrate. Our initial assumption is that the associated etching mechanism is due to a compositional difference between the core (MnO) and the shell (Mn_3O_4) of MONs.[11,22] However, X-ray photoelectron spectroscopy (XPS) analysis has revealed that the oxidation state of MONs is relatively unchanged despite the core removal during etchant treatment (Figure 4b), thus it implies that the core and shell are likely to be of the same oxidation state. For controls, encapsulated MONs were also separately immersed in phosphate buffered saline (PBS) and mild HCl solution (concentration diluted to ≈pH 5), but the resulting nanoparticles exhibit an absence of hollow morphology. This clearly suggests that the precise nanoscale etching of MONs in our system is only possible when two key conditions are fulfilled: the presence of acetate ions and a mildly acidic pH environment. Indeed, the role of acetate anions to produce hollow MONs via the Kirkendall effect has been demonstrated previously.[5] However, it appears that the provision of an acidic medium in our system has altered the nature of the etching mechanism. In this regard, we postulate that the acetate ions present in our choice of etchant solution are able to adsorb strongly onto the surface of MONs and stabilize the exterior layer from dissolution. As a result, the H^+ ions (acidic pH) will attack along the randomly distributed regions of high defect densities in the particle interior to form small cavities. During the course of the etching process, these interior cavities will gradually enlarge and coalesce, thereby causing a preferential removal of the MnO cores to form the hollow nanostructures. Finally, when regular aliquots of the solution are tested for their Mn concentration during the etching process, it can be observed that there is a gradual decline in the Mn content (Figure 4c). This shows that after the core dissolution, the interior Mn^{2+} ions can readily diffuse through the nanoreactor walls to prevent a toxic accumulation of Mn^{2+} ions within the framework, thus not impeding their use as T_1 MRI contrast agents for biomedical applications.

2.4. Assessment of Biocompatibility

Cytotoxicity of hollow MONs with multiple 16 nm cores was evaluated using the Alamar blue assay. **Figure 5** shows that more than 80% of the HeLa cells remained viable following 12 h incubation at a high nanoparticle concentration of 480 μg mL^{-1}. Based on inductive coupled plasma-atomic emission spectroscopy (ICP-AES), this corresponds to 0.448×10^{-3} M of Mn, which exceeds the dose concentration of 0.40×10^{-3} M used for the in vivo MR imaging of mouse in our study (Figure 2b). Hence, it indicates that the nanoparticles are relatively noncytotoxic at the concentration range required for sufficient MRI contrast sensitivity. The excellent biocompatibility of hollow MONs is due to the two constituent materials that form the nanoreactor backbone: nanostructured silica is an inert and

© 2015 WILEY-VCH Verlag GmbH & Co. KGaA, Weinheim

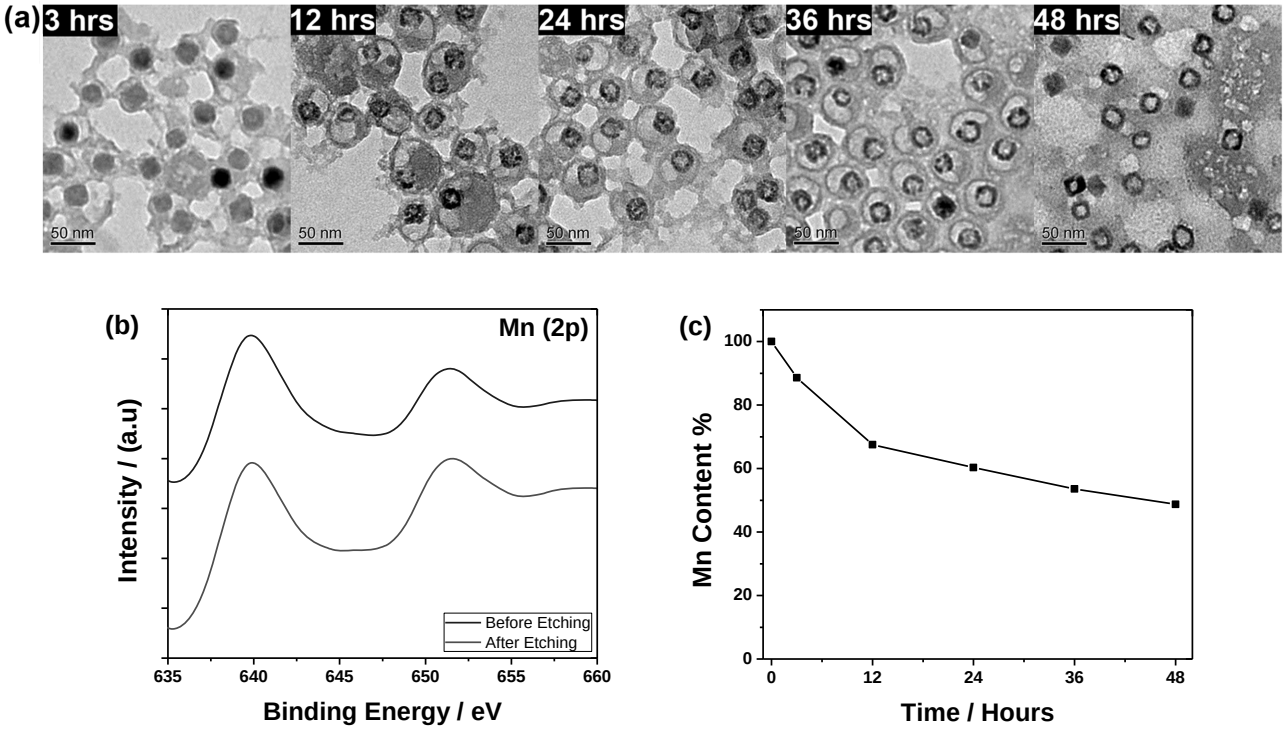

Figure 4. a) TEM images of the MONs dispersed in acetate buffer solution at different stages of the nanoscale etching process. b) High-resolution XPS scans of the Mn 2p region before and after the nanoscale etching process. (c) Evolution of the manganese content during the nanoscale etching of MONs.

biocompatible material that is commonly used for drug delivery and nanomedicine applications.[23,24] On the other hand, F127, being a PEO-based block copolymer, has been approved by FDA for parenteral administration and is widely used for pharmaceutical applications.[25,26]

Based on available reports in the literature on biodistribution studies with nanoparticles of similar size (50–100 nm) and composition (silica and PEO/PEG conjugates), the majority of such nanoparticles tend to accumulate in the mice liver and spleen due to the mononuclear phagocyte system that exists in these organs.[27,28] There was evidence of renal excretion as the nanostructured silica would biodegrade to form silicic acid or oligomeric silica species and be eliminated by the urinary system. Nonetheless, most of the nanoparticles were predominantly eliminated via the faecal and biliary excretion routes.[29] Consequently, one would envision the use of the hollow MONs as hepatobiliary-specific MR contrast agents since they would be readily taken up by functioning hepatocytes and excreted in the bile. Among the potential applications of these nanoparticles, they include the improvement of lesion detection in the liver and the mapping of the biliary anatomic structure using MR imaging.[30]

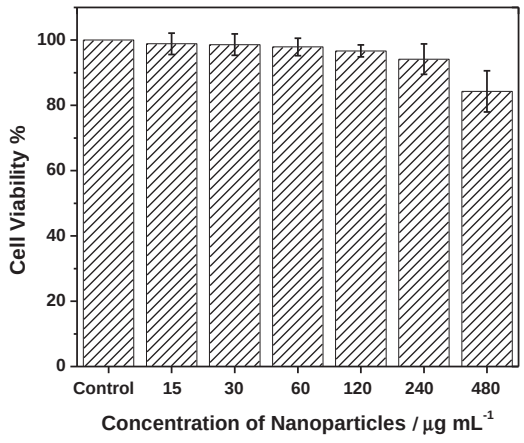

Figure 5. Viability of HeLa cells cultured in the presence of hollow MONs for 12 h.

3. Conclusion

We have designed and successfully developed a hybrid silica nanoreactor to encapsulate MONs with well-defined hollow nanostructures. Due to the incorporation of hydrophilic PEO-based polymer channels into the stable silica framework, it allows for the etching chemistry to be conducted in a confined volume under controlled conditions and selective permeability. More importantly, the silica nanoreactors are able to maintain their structural integrity and aqueous dispersity under the benign conditions of etchant treatment. The versatility of our synthesis protocol has been demonstrated by the successful formation of hollow MONs with different nanocomposite architectures. Herein, the correlation of various factors, such as the MON morphology (solid or hollow nanoparticles) and number of MONs (single or multiple) are analyzed and discussed. Although different nanostructural parameters can lead to positive contrast enhancement, there are distinct differences with

© 2015 WILEY-VCH Verlag GmbH & Co. KGaA, Weinheim

regard to the magnitude. In particular, we observed a significant increase in the r_1 relaxivity if an optimal number of MONs is encapsulated within the framework. Hence, it represents an alternative approach to design high-performance MON-based MRI contrast agents. Finally, we have proposed an alternative etching mechanism to highlight the essential roles of acetate ions and a mildly acidic pH for the precise nanoscale etching of MONs.

4. Experimental Section

Synthesis of MnO Nanoparticles: The preparation procedure for manganese oleate precursor and MONs was described in previously published reports.[31] Briefly, manganese oleate was first dissolved in 1-octadecene and degassed at 60 °C for 2 h. The reaction mixture was then heated to 300 °C under an argon atmosphere, and kept at this temperature for 1 h, before being cooled back to room temperature for subsequent precipitation and retrieval of MONs via centrifugation. The as-synthesized MONs were finally dispersed in THF solution at a concentration of 20 mg mL^{-1}. When the reaction was done in 1-hexadecene instead of 1-octadecene solvent at 280 °C for 1 h, MONs of size 16 nm were synthesized. Meanwhile, when the reaction was performed in 1-tetradecene solvent at 250 °C for 30 min, MONs of ≈8 nm in sizes were produced.

Encapsulation of MONs in Nanoreactor: An interfacial templating scheme was employed to fabricate the hybrid silica nanoreactor.[11] For single MON encapsulation, F127 (15 mg) was first dissolved in THF (450 µL). The MONs stock solution (450 µL) and TMOS (20 µL) were then added and stirred to obtain a homogeneous mixture. Next, the mixture solution was slowly injected into deionized water (10 g) while being stirred rapidly. Stirring was continued for an additional 4 d to ensure complete hydrolysis of TMOS. The resulting aqueous dispersion was dialyzed against deionized water to remove any unreacted silica precursors. Finally, the encapsulated MONs were retrieved by centrifuging at 6000 rpm, discarding the supernatant and redispersing the solid residue in deionized water. A similar protocol was used for multiple MONs encapsulation except for the following differences: 1) To prepare nanoreactors with an average of 3, 5 and 10 MONs, F127 (15 mg) was first dissolved in decreasing volumes of THF (300, 150, 0 µL) respectively. Next, increasing volumes of MONs stock solution (600, 750, 900 µL) were added accordingly so as to make up a total volume of 900 µL. 2) In the case of nanoreactors with an average of 5 and 10 MONs, they were retrieved by centrifuging at 4000 rpm, discarding the supernatant, and redispersing the solid residue in deionized water. The yield of nanoreactors with different number of MONs was determined based on a statistical assembly of 100 nanoparticles under TEM and can be found in Table S1 (Supporting Information).

Nanoscale Etching of Encapsulated MONs: To form the desired hollow core structure of MONs, the encapsulated MONs were dialyzed against an acetate buffer solution (pH 5.2) at room temperature for 36 h. During this process, small aliquots of the sample solution were also extracted and analyzed for their Mn contents by ICP-AES. The resulting hollow MONs were purified by repeated centrifugation and redispersion in deionized water. Finally, the solution was passed through a 0.20 µm filter to remove the presence of any aggregates.

Characterization: TEM (JEM-2010F, 200 kV) was employed to study the size and morphology of nanoparticles. DLS (Malvern Zetasizer Nanoseries) was performed using a HeNe laser (633 nm) to measure the particle size and distribution in solution. XRD (Bruker AXS D8 Advance) was conducted to identify the crystalline phase of MONs. Phase analyses were carried out under Cu Kα radiation (λ = 1.5406 Å) at a scanning rate of $2\theta = 2°$ min^{-1} over a range of $2\theta = 30°$–$80°$. XPS (ESCALAB 220I-XL Thermo Scientific) was employed to determine the oxidation state of MONs. ICP-AES was used to determine the manganese concentration in the samples.

MRI Relaxivity Measurement: MR relaxivities of the MONs and Magnevist were evaluated by using a 7-Tesla Bruker Clinscan MRI system. T_1 relaxation times were determined from an inversion recovery experiment with a number of TI (inversion time) (10 TIs; TI: 100–7000 ms; echo times (TE): 12 ms). The longitudinal (r_1) relaxivities were obtained from the slope of $1/T_1$ versus molar concentration plots.

In Vivo MR Imaging: Briefly, 1% agarose (200 µL) and MONs (0.40×10^{-3} M) (fixed with agarose) were injected into the left and right flanks of a nude (nu/nu, Balb/c) mouse, respectively. The mouse was placed in a 7-Tesla Bruker Clinscan MRI system under anesthetization by inhalation of isoflurane. The T_1-weighted images were acquired with the following acquisition parameters: repetition time (TR) and echo time (TE), TR/TE = 526.0/8.9 ms, with eight averages and field of view (FOV) = 40 mm. Animal experiments were performed in accordance with the Institutional Animal Care and Use Committee (IACUC) guidelines under ethics number IACUC 120748.

Cytotoxicity Study: The Alamar blue assay was performed to assess the cytotoxicity of hollow MONs with multiple 16 nm cores. Briefly, HeLa cells obtained from ATCC were cultured on a 96-well plate at a density of 6000 cells $well^{-1}$. After 24 h, fresh culture medium containing MONs with concentration range of 0–480 µg mL^{-1} was added. The cells were incubated with the nanoparticles at 37 °C in 5% CO_2 for 12 h, then rinsed and replaced with fresh culture medium. Alamar blue reagent was added to each well at a concentration of 10% (v/v) and the cells were incubated for an additional 4 h, followed by spectrophotometric analysis using a Fluoroskan Ascent FL spectrophotometer (Thermo Labsystems). Cell viability was determined as a percentage of the untreated control cells.

Supporting Information

Supporting Information is available from the Wiley Online Library or from the author.

Acknowledgements

This work was supported by the Agency for Science, Technology and Research (A*Star, Singapore), BMRC-SERC Joint Grant (Grant No. 112 1480002)

Received: March 30, 2015
Revised: May 23, 2015
Published online: July 24, 2015

[1] a) H. B. Na, J. H. Lee, K. An, Y. I. Park, M. Park, I. S. Lee, D.-H. Nam, S. T. Kim, S.-H. Kim, S.-W. Kim, K.-H. Lim, K.-S. Kim, S.-O. Kim, T. Hyeon, *Angew. Chem.* **2007**, *119*, 5493; b) *Angew. Chem. Int. Ed.* **2007**, *46*, 5397.

[2] R. Xing, F. Zhang, J. Xie, M. Aronova, G. Zhang, N. Guo, X. Huang, X. Sun, G. Liu, L. H. Bryant, A. Bhirde, A. Liang, Y. Hou, R. D. Leapman, S. Sun, X. Chen, *Nanoscale* **2011**, *3*, 4943.

[3] a) J. Shin, R. M. Anisur, M. K. Ko, G. H. Im, J. H. Lee, I. S. Lee, *Angew. Chem.* **2009**, *121*, 327; b) *Angew. Chem. Int. Ed.* **2009**, *48*, 321.

[4] T. Kim, E. Momin, J. Choi, K. Yuan, H. Zaidi, J. Kim, M. Park, N. Lee, M. T. McMahon, A. Quinones-Hinojosa, J. W. M. Bulte, T. Hyeon, A. A. Gilad, *J. Am. Chem. Soc.* **2011**, *133*, 2955.

[5] Y.-K. Peng, C.-W. Lai, C.-L. Liu, H.-C. Chen, Y.-H. Hsiao, W.-L. Liu, K.-C. Tang, Y. Chi, J.-K. Hsiao, K.-E. Lim, H.-E. Liao, J.-J. Shyue, P.-T. Chou, *ACS Nano* **2011**, *5*, 4177.

[6] K. H. Bae, K. Lee, C. Kim, T. G. Park, *Biomaterials* **2011**, *32*, 176.

[7] T.-L. Ha, H. J. Kim, J. Shin, G. H. Im, J. W. Lee, H. Heo, J. Yang, C. M. Kang, Y. S. Choe, J. H. Lee, I. S. Lee, *Chem. Commun.* **2011**, *47*, 9176.

© 2015 WILEY-VCH Verlag GmbH & Co. KGaA, Weinheim

[8] R. M. Anisur, J. Shin, H. H. Choi, K. M. Yeo, E. J. Kang, I. S. Lee, *J. Mater. Chem.* **2010**, *20*, 10615.
[9] K. An, S. G. Kwon, M. Park, H. B. Na, S.-I. Baik, J. H. Yu, D. Kim, J. S. Son, Y. W. Kim, I. C. Song, W. K. Moon, H. M. Park, T. Hyeon, *Nano Lett.* **2008**, *8*, 4252.
[10] M. F. Bennewitz, T. L. Lobo, M. K. Nkansah, G. Ulas, G. W. Brudvig, E. M. Shapiro, *ACS Nano* **2011**, *5*, 3438.
[11] B. Y. W. Hsu, M. Wang, Y. Zhang, V. Vijayaragavan, S. Y. Wong, A. Y. C. Chang, K. K. Bhakoo, X. Li, J. Wang, *Nanoscale* **2014**, *6*, 293.
[12] R. V. Roosbroeck, W. V. Roy, T. Stakenborg, J. Trekker, A. D'Hollander, T. Dresselaers, U. Himmelreich, J. Lammertyn, L. Lagae, *ACS Nano* **2014**, *8*, 2269.
[13] W. Baaziz, B. P. Pichon, S. Fleutot, Y. Liu, C. Lefevre, J.-M. Greneche, M. Toumi, T. Mhiri, S. Begin-Colin, *J. Phys. Chem. C* **2014**, *118*, 3795.
[14] M. A. Sieber, T. Steger-Hartmann, P. Lengsfeld, H. Pietsch, *J. Magn. Reson. Imaging* **2009**, *30*, 1268.
[15] M. R. Prince, H. L. Zhang, J. C. Prowda, M. E. Grossman, D. N. Silvers, *Radiographics* **2009**, *29*, 1565.
[16] N. Bloembergen, L. O. Morgan, *J. Chem. Phys.* **1961**, *14*, 842.
[17] A. Bjornerud, The Physics of Magnetic Resonance Imaging, FYS-KJM 4740 Lecture Notes, February 2015.
[18] P. Caravan, C. T. Farrar, L. Frullano, R. Uppal, *Contrast Media Mol. Imaging* **2009**, *4*, 89.
[19] Z. Cheng, D. L. J. Thorek, A. Tsourkas, *Adv. Funct. Mater.* **2009**, *19*, 3753.
[20] Y. Yin, C. K. Erdonmez, A. Cabot, S. Hughes, A. P. Alivisatos, *Adv. Funct. Mater.* **2006**, *16*, 1389.
[21] Z. Yang, N. Yang, J. Yang, J. Bergström, M.-P. Pileni, *Adv. Funct. Mater.* **2015**, *25*, 891.
[22] a) T. Kim, E.-J. Cho, Y. Chae, M. Kim, A. Oh, J. Jin, E.-S. Lee, H. Baik, S. Haam, J.-S. Suh, Y.-M. Huh, K. Lee, *Angew Chem.* **2011**, *123*, 10777; b) *Angew. Chem. Int. Ed.* **2011**, *50*, 10589.
[23] C. Barbé, J. Bartlett, L. Kong, K. Finnie, H. Q. Lin, M. Larkin, S. Calleja, A. Bush, G. Calleja, *Adv. Mater.* **2004**, *16*, 1959.
[24] Y. Piao, A. Burns, J. Kim, U. Wiesner, T. Hyeon, *Adv. Funct. Mater.* **2008**, *18*, 1.
[25] M. L. Adams, A. Lavasanifar, G. S. Kwon, *J. Pharm. Sci.* **2003**, *92*, 1343.
[26] W. Zhang, K. Gilstrap, L. Wu, K. C. R. Bahadur, M. A. Moss, Q. Wang, X. Lu, X. He, *ACS Nano* **2010**, *4*, 6747.
[27] H. Hu, A. Dai, J. Sun, X. Li, F. Gao, L. Wu, Y. Fang, H. Yang, L. An, H. Wu, S. Yang, *Nanoscale* **2013**, *5*, 10447.
[28] X. Yang, Z. Zhou, L. Wang, C. Tang, H. Yang, S. Yang, *Mater. Res. Bull.* **2014**, *57*, 97.
[29] J.-A. Lee, M.-K. Kim, H.-J. Paek, Y.-R. Kim, M.-K. Kim, J.-K. Lee, J. Jeong, S.-J. Choi, *Int. J. Nanomedicine* **2014**, *9*, 251.
[30] M. K. Seale, O. A. Catalano, S. Saini, P. F. Hahn, D. V Sahani, *RadioGraphics* **2009**, *29*, 1725.
[31] T. D. Schladt, T. Graf, W. Tremel, *Chem. Mater.* **2009**, *21*, 3183.

© 2015 WILEY-VCH Verlag GmbH & Co. KGaA, Weinheim